Volume 19
Number 8
28 April 2026
Pages 2387–2736

Energy & Environmental Science

rsc.li/ees

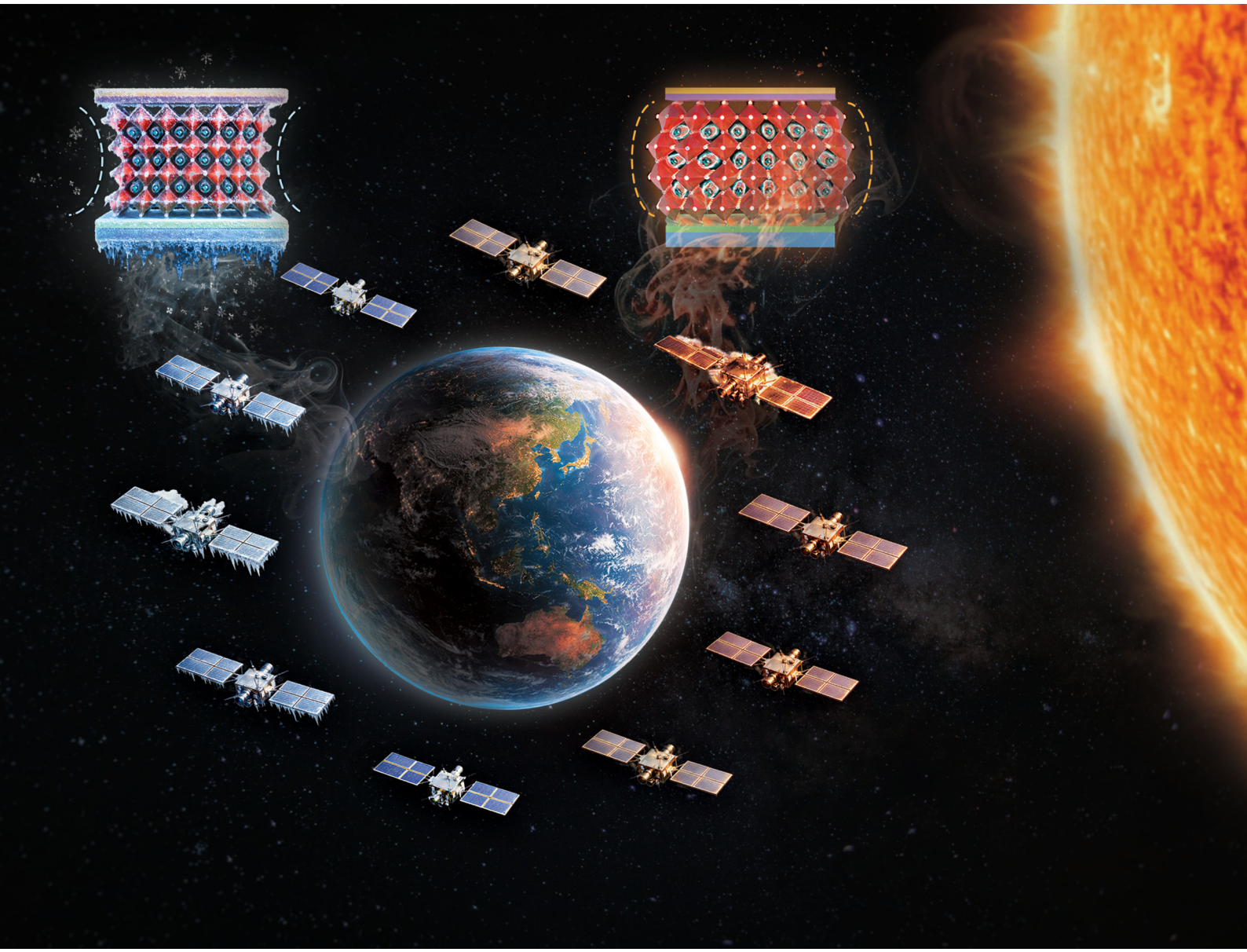

ISSN 1754-5706

ROYAL SOCIETY OF CHEMISTRY

PAPER

Xiaojing Hao, Dohyung Kim, Helen Hejin Park, Jae Sung Yun *et al.*
Towards space compatible perovskite solar cells: guidelines for thermal shock resilience and near space balloon testing

Energy & Environmental Science

ROYAL SOCIETY OF CHEMISTRY

PAPER

View Article Online
View Journal | View Issue

Cite this: *Energy Environ. Sci.*, 2026, **19**, 2557

Towards space compatible perovskite solar cells: guidelines for thermal shock resilience and near space balloon testing

Minwoo Lee, †[a] George Kwesi Asare,†[bc] Tommy H. Richards,[d] Dong Gyu Lee,[e] Tae Kyung Lee,[ef] Jongsung Park,[g] Juhong Oh,[h] Jihoo Lim,[a] Martin A. Green,[a] Xiaojing Hao,*[a] Dohyung Kim,*[ij] Helen Hejin Park *[bck] and Jae Sung Yun*[dl]

Received 1st July 2025,
Accepted 9th February 2026

DOI: 10.1039/d5ee03704b

rsc.li/ees

Perovskite solar cells (PSCs) are promising candidates for space applications due to their high efficiency, radiation tolerance, and high power-to-mass ratio. However, the harsh space environment introduces stressors such as thermal shock (TS) from rapid temperature transitions in orbit, a degradation mode that remains underexplored. This study investigated the real operating temperature profiles experienced by solar cells orbiting in low Earth orbit, revealing rapid and extreme temperature transitions. Based on these findings, we developed an accelerated TS testing protocol, cycling PSC devices between −80 °C and +80 °C at a rapid ramp rate of 16 °C min^{-1} for 100 cycles, designed to replicate and amplify the stresses induced by actual orbital thermal cycles. Using $FAPbI_3$ as a model system, we explored the impact of varying concentrations of $MAPbBr_3$ (0–7%) on the perovskite film's structural stability under this accelerated TS. Our results indicate that an intermediate $MAPbBr_3$ incorporation level (specifically 5%) most effectively suppresses microstrain and the formation of the detrimental δ-phase after TS exposure. To validate our laboratory findings under near-space conditions, we conducted a comparative high-altitude balloon test at 35 km. These findings establish TS as a critical testing framework for evaluating PSC stability in space applications and highlight the necessity of refining material compositions for space applications.

Broader context

Perovskite solar cells (PSCs) have advantages of lightweight, high-efficiency, and cost-effective photovoltaic solutions that are particularly attractive for emerging space technologies such as CubeSats and high-altitude platforms. However, the extreme thermal conditions in low Earth orbit (LEO), characterized by rapid temperature fluctuations, pose a significant threat to device stability and long-term performance. Existing terrestrial testing protocols fail to replicate the high ramp rates and broad temperature swings experienced in orbit. In this work, we introduce an accelerated thermal shock protocol that simulates the realistic orbital thermal environment, enabling rapid evaluation of degradation mechanisms. We demonstrate that $MAPbBr_3$ incorporation into $FAPbI_3$ can significantly enhance thermal resilience under these extreme conditions. This study bridges the gap between lab-scale perovskite research and real-world deployment in aerospace environments, offering key insights for the future qualification of PSCs in space missions.

[a] *Australian Centre for Advanced Photovoltaics (ACAP), School of Photovoltaic and Renewable Energy Engineering, University of New South Wales, Sydney, NSW 2052, Australia. E-mail: xj.hao@unsw.edu.au*
[b] *Advanced Materials Division, Korea Research Institute of Chemical Technology (KRICT), Daejeon, 34114, Republic of Korea. E-mail: hhpark@krict.re.kr*
[c] *Department of Advanced Materials and Chemical Engineering, University of Science and Technology (UST), Daejeon, 34113, Republic of Korea*
[d] *Department of Electrical and Electronic Engineering, Advanced Technology Institute (ATI), University of Surrey, Guildford, Surrey GU2 7XH, UK. E-mail: j.yun@surrey.ac.uk*
[e] *Department of Materials Engineering and Convergence Technology, Gyeongsang National University, Jinju, 52828, Republic of Korea*
[f] *School of Materials Science and Engineering, Gyeongsang National University, Jinju, 52828, Republic of Korea*
[g] *Department of Energy Engineering, Future Convergence Technology Research Institute, Gyeongsang National University, Jinju, 52828, Republic of Korea*
[h] *Korea Testing Laboratory (KTL) Space Testing Center, 16, Sangdae-ro 72 beon-gil, Jinju-si, Gyeongsangnam-do, 52852, Republic of Korea*
[i] *Department of Advanced Materials Engineering, Chungbuk National University, Cheongju, Chungbuk 28644, Republic of Korea. E-mail: dohyungkim@chungbuk.ac.kr*
[j] *Department of Urban, Energy, Environment Engineering, Chungbuk National University, Cheongju, Chungbuk 28644, Republic of Korea*
[k] *Department of Chemical and Biological Engineering, Hanbat National University, Daejeon, 34158, Republic of Korea. E-mail: hhpark@hanbat.ac.kr*
[l] *Korea Institute of Science and Technology (KUKIST), Graduate School of Converging Science and Technology, Korea University, Seoul 02841, Republic of Korea*
† M. L and G. K. A. contributed equally to this work.

Introduction

Perovskite solar cells (PSCs) have emerged as promising candidates for space-based photovoltaics due to their high power-to-weight ratio, solution processability, and intrinsic radiation tolerance.[1–5] These features are particularly advantageous for small satellite platforms such as CubeSats, where payload constraints are stringent. However, the harsh space environment imposes additional stressors beyond radiation, including high vacuum,[6] UV exposure[7] and thermal shock (TS)[8] caused by rapid temperature transitions in orbit. Among these, TS remains one of the most underexplored degradation modes for PSCs.

On Earth, device stability is typically evaluated using thermal cycling tests such as IEC 61215, which prescribes ramping between −45 °C and +85 °C at rates below 2 °C min^{-1}.[9] While effective for terrestrial conditions, such protocols do not reflect the temperature fluctuations encountered in low Earth orbit (LEO), where satellites experience around 15 sunlight–eclipse transitions daily (around 5475 cycles per year) by Kepler's third law. These transitions induce sharp temperature gradients, often exceeding 5–6 °C min^{-1}, and can generate substantial mechanical strain in thin-film devices.[10,11] Unlike ground-based tests, LEO transitions occur on sub-hour timescales, where thermal expansion mismatches, lattice fatigue, and phase destabilization can lead to accelerated material degradation.[12]

For TS testing to realistically capture these stressors, two factors must be considered simultaneously which are the temperature range (ΔT) and the ramping rate (dT/dt). Wider ranges and faster ramps lead to higher thermal strain rates, which exacerbate mechanical failure and phase instability for perovskites structure. Despite these conditions, there is currently no standardized protocol for evaluating PSC resilience under space-relevant TS. Therefore, we first analyzed the temperature profiles experienced by satellites in LEO. Data from missions such as NOAA-21[13] revealed temperature ranges of approximately −90 °C to +80 °C and maximum heating rates up to 6.77 °C min^{-1}, significantly exceeding the around 1.67 °C min^{-1} ramp rate specified in terrestrial IEC 61215 protocols. Based on these findings, we implemented an accelerated TS testing protocol that cycles devices between −80 °C and +80 °C at a ramp rate of 16 °C min^{-1} for 100 cycles. While broader than typical orbital fluctuations, this protocol serves as a simplified accelerated proxy, designed to amplify thermal stress accumulation and reveal latent failure modes relevant to long-term space deployment.

Under TS conditions, perovskite films undergo rapid strain excursions that can deform the lattice and trigger phase transitions. Shen *et al.* showed that illumination on/off (day-night) cycling with modest ΔT accelerates degradation *via* periodic reformation of lattice strain, mitigated by phenylselenenyl chloride.[14] Chen *et al.* examined high-cycle terrestrial thermal cycling and reported severe microstrain accumulation, with endurance improved by an *n*-octylammonium iodide stress-management layer.[15] A concise comparison of operational regimes, temperature ranges, and mitigation strategies in these studies *versus* our rapid TS approach is provided in Table S1.

In this work, we use $FAPbI_3$ as a model system and apply a rapid TS protocol while tuning the incorporation of $MAPbBr_3$ (0–7%). Although cesium (Cs) is widely used to stabilize FA-based perovskites,[16] its smaller A-site radius shifts the tolerance factor and can complicate FA-Cs crystallization (multiple intermediate and local inhomogeneity), potentially introduce lattice strain unless carefully optimized.[17] By contrast, limited $MAPbBr_3$ incorporation provides concurrent A-site (MA^+) and halide (Br^-) substitution that promotes rapid α-phase formation/retention under fast ΔT. Within our TS protocol, the 5% $MAPbBr_3$ composition most effectively suppressed microstrain and δ-phase formation. To complement the laboratory protocol, we conducted a high-altitude balloon (HAB) campaign at approximately 35 km. We note that the HAB flight represents a distinct thermal regime from the laboratory TS protocol: whereas the TS protocol simulates the rapid, repetitive thermal cycling characteristic of orbital, satellite-like conditions, the HAB flight subjects devices to a single, slower thermal transient governed by atmospheric lapse rates. Consequently, the HAB test is not intended to replicate orbital thermal shock, but rather to validate device robustness under a complex, real-world near-space environment (low pressure, elevated UV, and partial AM0 irradiance) which is difficult to simulate simultaneously in the laboratory. Thus, the HAB test complements the TS study by evaluating whether the material optimizations identified under rapid thermal cycling remain effective when exposed to this multi-stressor profile.

Results and discussion

For small satellites, including CubeSats, which rely heavily on solar panels for power, maintaining solar cell integrity and efficiency is crucial. Temperature variations can significantly degrade performance, reducing power output and affecting mission operation. CubeSats are typically designed for missions lasting several months to years, making thermal resilience essential. Ensuring solar cells can withstand extreme temperature fluctuations enhances their lifespan and reliability, ultimately contributing to mission success.

In space, CubeSat solar cells experience substantial temperature variations as they transition between sunlit and eclipse phases during orbit, as illustrated in Fig. 1a. Theoretically, temperatures can drop below −100 °C in eclipse and exceed +100 °C under direct sunlight.[27] In alignment with such extremes, the European Cooperation for Space Standardization (ECSS) recommends a qualification range of −175 °C to +125 °C under protocol ECSS-E-ST-20-08C, typically across 100 to 1000 thermal cycles.[28] However, actual on-orbit temperature measurements are often less severe, constrained by mission-specific conditions (Table S2). As shown in Fig. 1b, surface temperatures recorded from satellites in LEO exhibit a range strongly influenced by orbital altitude and configuration. For instance, the TURKSAT-3USAT CubeSat reported the highest observed temperature of approximately +80 °C, while the NOAA-21 satellite recorded a minimum of approximately −90 °C.

These values indicate that, in practice, LEO satellites rarely exceed the ±100 °C thermal boundary. Variations in orbital parameters, including inclination, eclipse duration, and local solar time, affect the length and intensity of solar exposure. Satellite attitude control systems further modulate solar incidence on photovoltaic surfaces. In addition, onboard thermal control elements such as radiators, multilayer insulation, heat pipes, and heaters help regulate internal heat distribution.[29] Active payload operations, such as continuous communication or power-intensive instrumentation, can also contribute internal heat loads, mitigating the impact of radiative cooling.[30] Consequently, even satellites at comparable altitudes may undergo significantly different thermal profiles than predicted by theoretical models or qualification standards. Fig. 1c compares the temperature range with actual recorded LEO surface temperatures and the thermal shock protocol employed in this study. While the ECSS envelope spans from −175 °C to +125 °C, operational data indicate that the typical temperature range experienced by LEO satellites falls between approximately −90 °C and +80 °C. Notably, most satellites operate within a narrower thermal window of about −40 °C to +60 °C. The TS test range employed in this study (−80 °C to +80 °C) thus reflects a realistic worst-case scenario and provides a mission-relevant protocol for evaluating the thermal stability of perovskite solar cells under space-representative conditions.

Another critical parameter in the thermal qualification of space-based solar cells is the temperature ramp rate, the rate at which the satellite transitions between sunlit and eclipse regions during orbit, as illustrated in Fig. 2a. These rapid transitions can impose thermal shock, particularly at interfaces between materials with different coefficients of thermal expansion. In perovskite solar cells, this can lead to cumulative damage, including morphological degradation, interfacial delamination, and reduced photovoltaic performance, making thermal resilience a vital metric for space reliability.

Since satellites in LEO travel at a nearly constant orbital speed at a given altitude, their orbital period can be accurately calculated using Kepler's third law, as shown in Table S3. For our thermal shock testing protocol, we defined a test window of ±80 °C. Using this range, we calculated the corresponding thermal transition rates from sunlight to eclipse across different LEO altitudes (Fig. 2b). At 200 km, the rate is approximately 3.71 °C min^{-1}, which progressively decreases with altitude due to longer orbital durations.

Complementing this calculation, Fig. 2c presents real-time flight data from the NOAA-21 satellite at an altitude of 824 km, obtained *via* the integrated calibration/validation system.[13] The heating rate during eclipse exit (dark to sun) was observed to be 6.77 °C min^{-1}, while the cooling rate from sunlight to eclipse was 1.89 °C min^{-1}. This asymmetry reflects the fundamental thermal physics of space that heating is rapid due to direct solar irradiation in the absence of atmospheric damping, whereas cooling is slower due to radiative heat loss to deep space. Such asymmetry must be considered in the design and testing of thermally sensitive devices like perovskite solar cells.

Since the thermal ramp rate varies depending on satellite design, orbit geometry, and operational conditions, it is difficult to generalize. Therefore, we adopted a conservative, accelerated protocol with a ramp rate of 16 °C min^{-1} between −80 °C and +80 °C. This value, shown in Fig. 2d, exceeds the orbital heating rate of NOAA-21 by more than a factor of two, allowing us to intensify the thermal stress and probe latent failure mechanisms in perovskite devices. Finally, Fig. 2e compares our protocol to standard terrestrial conditions defined in IEC

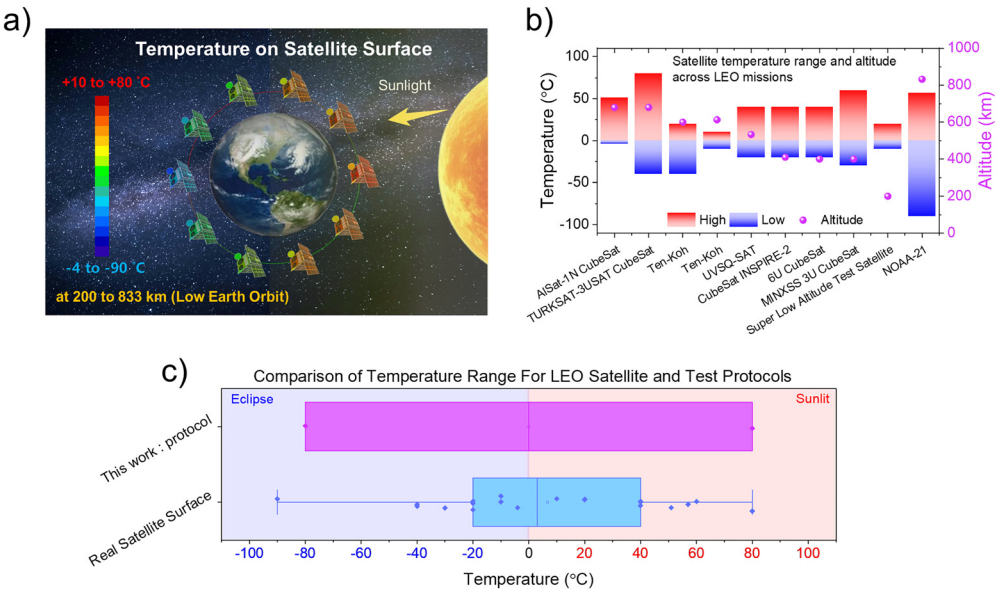

Fig. 1 (a) Illustration of the TS in a CubeSat in LEO, demonstrating the effects of both rotation and orbital motion as the CubeSat transitions between sunlight and eclipse regions. (b) Satellite surface temperature extremes and orbital altitudes across LEO missions.[13,18–26] (c) Comparison of temperature range for LEO satellite and test protocols.

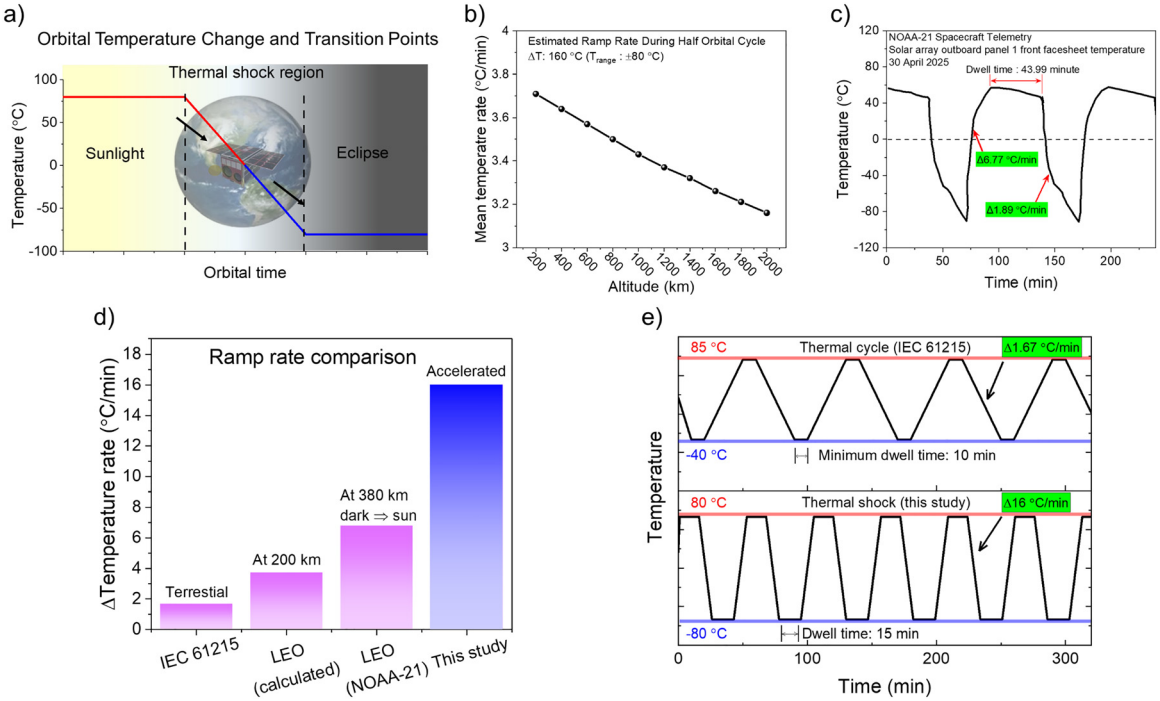

Fig. 2 (a) Schematic illustration of thermal shock occurring during orbital transitions between sunlight and eclipse in LEO. (b) Calculated thermal transition rates from sunlight to eclipse at varying altitudes (200–2000 km), assuming a ±80 °C temperature swing. (c) Real-time surface temperature profile of the NOAA-21 satellite measured on 30 April 2025. (d) Comparison of temperature ramp rates used in different test protocols and real-world conditions. (e) Line profile of IEC 61215 thermal cycling protocol, typically used for terrestrial solar cell qualification, highlighting the slower thermal gradient compared to our accelerated space-relevant protocol.

61215, which typically uses ramp rates around 1.67 °C min^{-1}. While suitable for ground-based qualification, these protocols do not account for the unique and more abrupt thermal transitions encountered in space. In the absence of standardized protocols for in-orbit thermal shock testing, our use of a 16 °C min^{-1} ramp rate provides a robust accelerated stress condition that enables a meaningful assessment of device durability and thermal robustness under harsh orbital environments.

$FAPbI_3$ perovskite was selected as the model system for this study due to its high power conversion efficiency, exceeding 27%,[31] which positions it as a promising candidate for space-based photovoltaics. However, the α-phase of $FAPbI_3$, crucial for efficient solar cell operation, is thermodynamically unstable at room temperature, necessitating strategies for phase stabilization.[32] Given the demonstrated effectiveness and widespread use of $MAPbBr_3$ as a dopant for stabilizing the α-phase of $FAPbI_3$,[33] we systematically investigated the impact of varying $MAPbBr_3$ ratios within the $FAPbI_3$ as a representative model system to validate our accelerated thermal shock protocol.

Following the TS tests, perovskite films experienced continuous compressive and tensile strains, leading to structural decomposition and performance degradation. This clearly indicates the key necessity for strategies to maintain lattice stability in extreme thermal environments. To investigate the fundamental mechanisms behind these effects, we conducted a molecular dynamics (MD) simulation (Fig. 3a), which provides time-resolved insights into the structural behavior of $FAPbI_3$ at −80 °C, 25 °C, and 80 °C. At −80 °C, the perovskite lattice exhibits minimal atomic fluctuations and a compact structure, with reduced lattice dimensions and angles compared to 25 °C. As the temperature rises to 25 °C, lattice constants and total potential energy steadily increase, accompanied by more pronounced atomic reorientations. At 80 °C, fluctuations became significantly more evident, with substantial octahedral tilting of the PbI_6 framework and more significant FA ion displacements (Fig. 3b). Further supporting these observations, Fig. S1 shows progressive disorder in lattice parameters under thermal stress.

To mitigate the structural instability induced by thermal fluctuations, we explored the role of $MAPbBr_3$ in suppressing δ-phase formation and improving the electronic uniformity of $FAPbI_3$. As earlier literature reported,[34] our findings indicate that while $MAPbBr_3$ incorporation effectively suppresses δ-phase formation, its impact on the crystallinity of the α-phase is more complex. To isolate this effect from annealing influences, we prepared perovskite films with 0% and 3% $MAPbBr_3$ by drying them under a vacuum (Fig. S2). As shown in Fig. S3, XRD data confirms a significant δ-phase presence in the 0% $MAPbBr_3$ sample, while the 3% $MAPbBr_3$ film exhibited a dominant α-phase signal with minimal δ-phase. However, the full width at half maximum (FWHM) of the α-phase peak increased from 0.162 (0%) to 0.188 (3%), which correlates with a decrease in grain size. This peak broadening is primarily attributed to the Scherrer effect due to smaller grain sizes in the

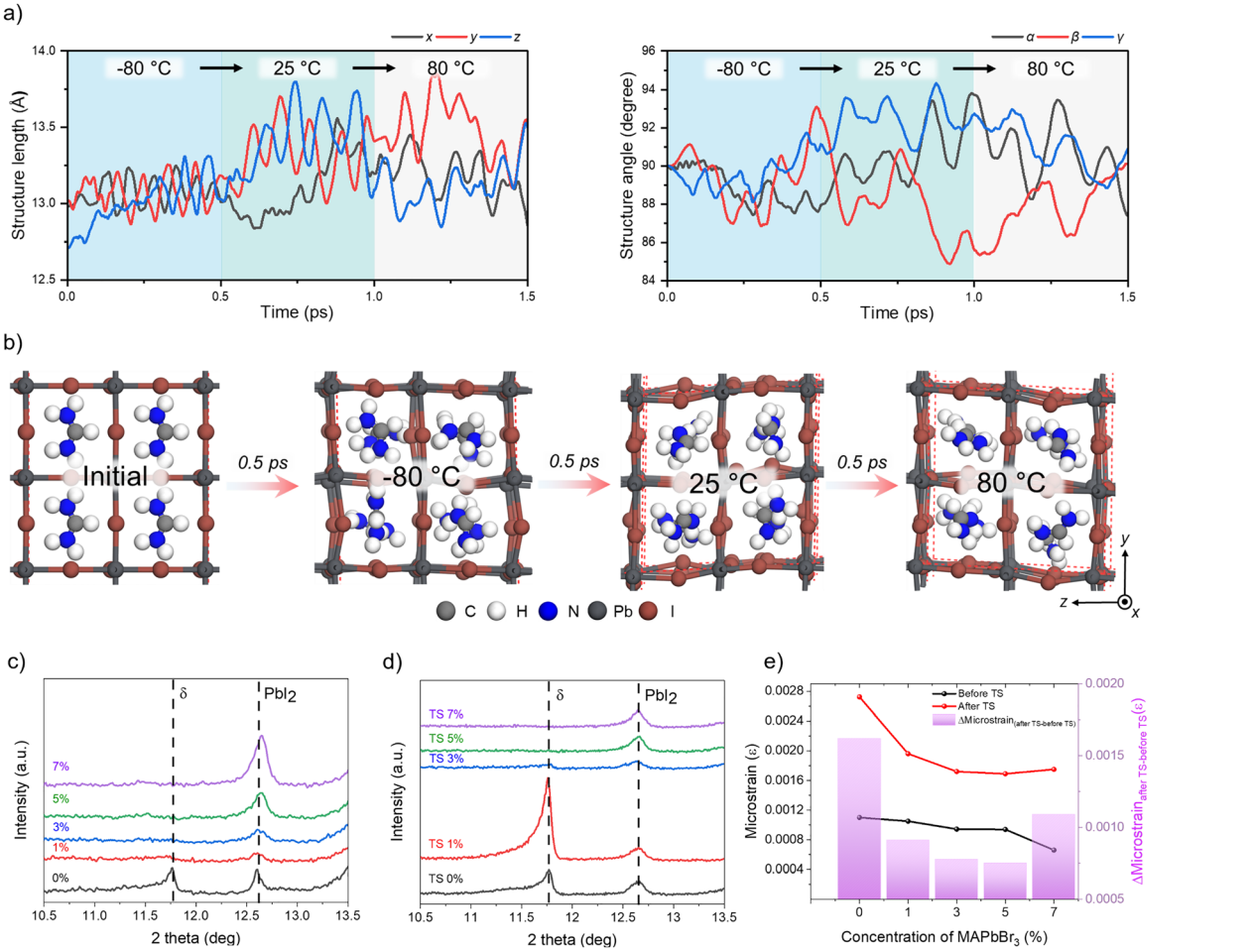

Fig. 3 MD simulation for (a) the structure length and angle and (b) the structure of $FAPbI_3$ according to temperature conditions and simulation times. XRD patterns of $FAPbI_3$ with $MAPbBr_3$ incorporation ranging from 0% to 7% (c) before and (d) after the TS test. (e) Comparison of micro-strain before and after TS.

3% $MAPbBr_3$ sample, confirmed by KPFM in Fig. S4, while localized lattice strain from Br incorporation may further contribute to structural distortion.[35] Despite this increase in FWHM, KPFM measurements reveal a more uniform CPD distribution in the 3% $MAPbBr_3$ sample, whereas the 0% sample exhibits a nonhomogeneous work function with a shoulder peak due to the δ-phase, as shown in Fig. S4. This suggests that while localized strain and grain size reduction are present in the 3% $MAPbBr_3$ film, its surface electronic uniformity is improved due to suppressed δ-phase formation. These results highlight the necessity of optimizing $MAPbBr_3$ incorporation to balance structural integrity, electronic homogeneity, and charge transport properties.

Building on these findings, we further examined the stability of annealed perovskite films under TS conditions to evaluate the long-term stabilizing effects of $MAPbBr_3$. Using XRD measurements before and after 100 TS cycles (−80 °C to +80 °C), we explored a range of $MAPbBr_3$ concentrations (0%, 1%, 3%, 5%, and 7%) to elucidate how $MAPbBr_3$ contributes to the structural and phase stability of $FAPbI_3$ under extreme thermal stress. XRD patterns (Fig. 3c and d) reveal variations in δ-phase and PbI_2 peaks before and after TS tests. A broader set of XRD patterns and variation of FWHM are provided in Fig. S5. Initially, Fig. 3c shows that the pure $FAPbI_3$ film (0% $MAPbBr_3$) exhibits peaks corresponding to both the δ-phase, an undesirable orthorhombic form, and PbI_2. However, 1% $MAPbBr_3$ significantly suppressed the δ-phase, stabilizing the α-phase. At higher $MAPbBr_3$ concentrations, increased PbI_2 intensity was observed, likely due to local structural imbalances from Br^- substitution for I^- ions and partial phase separation.[36] This suggests that moderate $MAPbBr_3$ concentrations enhance the α-phase's structural stability, whereas excessive concentrations may require optimization to minimize secondary phases. The stronger Pb–Br bond compared to Pb–I bond[37] contributes to improved thermal and phase stability by inducing subtle lattice contraction, reducing octahedral tilting, and enhancing structural coherence. Additionally, Br^- has been reported to exhibit lower ion mobility than I^-, which potentially mitigates ion migration under thermal stress and supports enhanced stability.[38]

Subsequently, we assessed the impact of TS on phase stability with varying $MAPbBr_3$ concentrations. As shown in

the XRD patterns in Fig. 3d, the 0% sample exhibited a slight increase in δ-phase intensity after TS, indicating partial decomposition. Although we expected $MAPbBr_3$ to mitigate these effects, the 1% $MAPbBr_3$ sample showed a substantial increase in δ-phase content after TS. This unexpected result suggests that low $MAPbBr_3$ concentrations may not offer sufficient protection against TS. In contrast, films with 3% or higher $MAPbBr_3$ concentrations showed no increase in δ-phase or PbI_2 peaks following TS. This suggests that there is an optimal concentration threshold, above which $MAPbBr_3$ effectively enhances TS resistance in $FAPbI_3$.

Further insights into the structural stability of the perovskite films are provided by the micro-strain analysis (Fig. 3e), based on XRD results. The sample without $MAPbBr_3$ (0%) showed a notable increase in micro-strain, by approximately 0.0016 after TS. In contrast, among the $MAPbBr_3$-incorporated samples, the sample with 5% $MAPbBr_3$ concentration exhibited the smallest micro-strain variation (0.00075) after TS, indicating better structural stability. The complete set of XRD data, including FWHM variations and Williamson–Hall plots, is provided in Fig. S5 and S6. This observation aligns with SEM analysis (Fig. S7), where pinhole formation in perovskite films was observed following TS for the 1% $MAPbBr_3$ film. Interestingly, as the $MAPbBr_3$ concentration increased, the number of pinholes decreased, suggesting that $MAPbBr_3$ stabilizes the perovskite phase and enhances morphological integrity. Furthermore, cross-sectional SEM images (Fig. S8) confirm that these morphological changes are confined to the surface of the perovskite layer, with no observable alterations in the bulk structure and delimitation.

To further investigate, we analyzed the influence of surface roughness on strain evolution, as smoother surfaces with fewer irregularities tend to exhibit reduced strain accumulation, thereby mitigating the impact of rapid thermal fluctuations.[39] As shown in Fig. S9, the incorporation of $MAPbBr_3$ results in a smoother perovskite surface with lower RMS roughness, while the three-dimensional morphology in Fig. S10 further confirms a more uniform and compact structure. The incorporation of $MAPbBr_3$ modifies crystallization kinetics, promoting a more homogeneous morphology. Fig. S11 compares the height distribution before and after the TS. It shows that the 3% and 5% $MAPbBr_3$ samples exhibit significantly lower height variation after TS compared to other compositions, indicating reduced structural distortion. Consequently, the microstrain variation in these samples is also minimized, as confirmed by Fig. 3e.

After analyzing the impact of TS on the crystalline and structural changes in $FAPbI_3$ with varying $MAPbBr_3$ concentrations, we explored nanoscale CPD spatial maps measured by KPFM. As shown in Fig. 4a and b, under dark and light conditions during the KPFM measurement for the 1% and 5% $MAPbBr_3$ incorporated samples with TS, certain grains display noticeably brighter CPD signals (marked by green circles) despite exhibiting similar morphology to regular grains. The bright CPD grains were absent in pre-TS samples (see Fig. S12), indicating that the abrupt temperature variations from TS likely induced them. These bright CPD grains are unusual as they have higher CPD, which refers to shifting the Fermi level to the valence band. Interestingly, as the concentration of $MAPbBr_3$ increased, the number of bright CPD grains decreased (Fig. S13). Bright CPD grains were predominantly observed in samples with lower $MAPbBr_3$ concentrations.

After TS, the 1% $MAPbBr_3$ sample exhibited a significant increase in bright CPD grains, while the 5% sample showed fewer grains. Since bright CPD grains indicate localized variations in charge potential, often correlated with defect sites, the higher distribution of these grains in the 1% $MAPbBr_3$ sample suggests greater defect formation due to TS. In contrast, the 5% $MAPbBr_3$ sample showed a more uniform CPD distribution, indicating better charge homogeneity and fewer defect-induced variations, as shown in Fig. S14. When comparing surface photovoltage (SPV) values, as shown in Fig. 4c, the 5% $MAPbBr_3$ sample exhibited a higher SPV for regular CPD grains, measuring 0.383 V, compared to 0.096 V for the 1% sample. This higher SPV suggests more efficient charge extraction, supporting the conclusion that the 5% $MAPbBr_3$ composition better maintains charge transport pathways even after TS exposure.

For bright CPD grains (Fig. 4d), the SPV in the 5% sample was measured at 0.260 V, whereas the 1% sample showed 0.101 V. Although these regions typically indicate structural inhomogeneity, the 5% $MAPbBr_3$ sample still exhibited higher SPV, suggesting improved charge transport characteristics compared to the 1% counterpart. These findings align with the MD simulations (Fig. 3a and b), which indicate that FA ion displacement contributes to lattice instability in $FAPbI_3$, potentially leading to defect formation in the 1% $MAPbBr_3$ sample. In contrast, the incorporation of higher $MAPbBr_3$ concentrations appears to mitigate these structural instabilities, resulting in fewer defect sites after TS.

The reduced distribution of bright CPD grains and the higher SPV values in the 5% $MAPbBr_3$ sample further suggest lower defect generation from TS and greater structural stability. This mechanism is schematically illustrated in Fig. 4e, where repeated thermal expansion and contraction cycles induce structural distortions in the perovskite lattice, leading to the formation of recombination sites within the bright CPD grains. The ability of the 5% $MAPbBr_3$ sample to suppress these thermally induced recombination centers highlights its enhanced resilience to TS-induced degradation.

Additionally, we analyzed the CPD distribution across the entire area of the scanned CPD images before and after TS for the 1% and 5% $MAPbBr_3$ samples in the dark condition. As shown in Fig. 4f, the CPD results for the 1% $MAPbBr_3$ sample indicate that the FWHM increased by approximately 0.068 after TS, indicating a decrease in the homogeneity of the work function across the film. Moreover, the mean CPD value negatively shifted by 0.270 V after TS, highlighting reduced hole density on the surface with the significant recombination sites. In contrast, for the 5% $MAPbBr_3$ sample, Fig. 4g shows that the FWHM change was notably smaller, with an increase of only 0.052, while the mean CPD shifted positively to approximately 0.135 V.

These findings confirm that TS significantly affects the work function of perovskite films, primarily due to the reduced phase

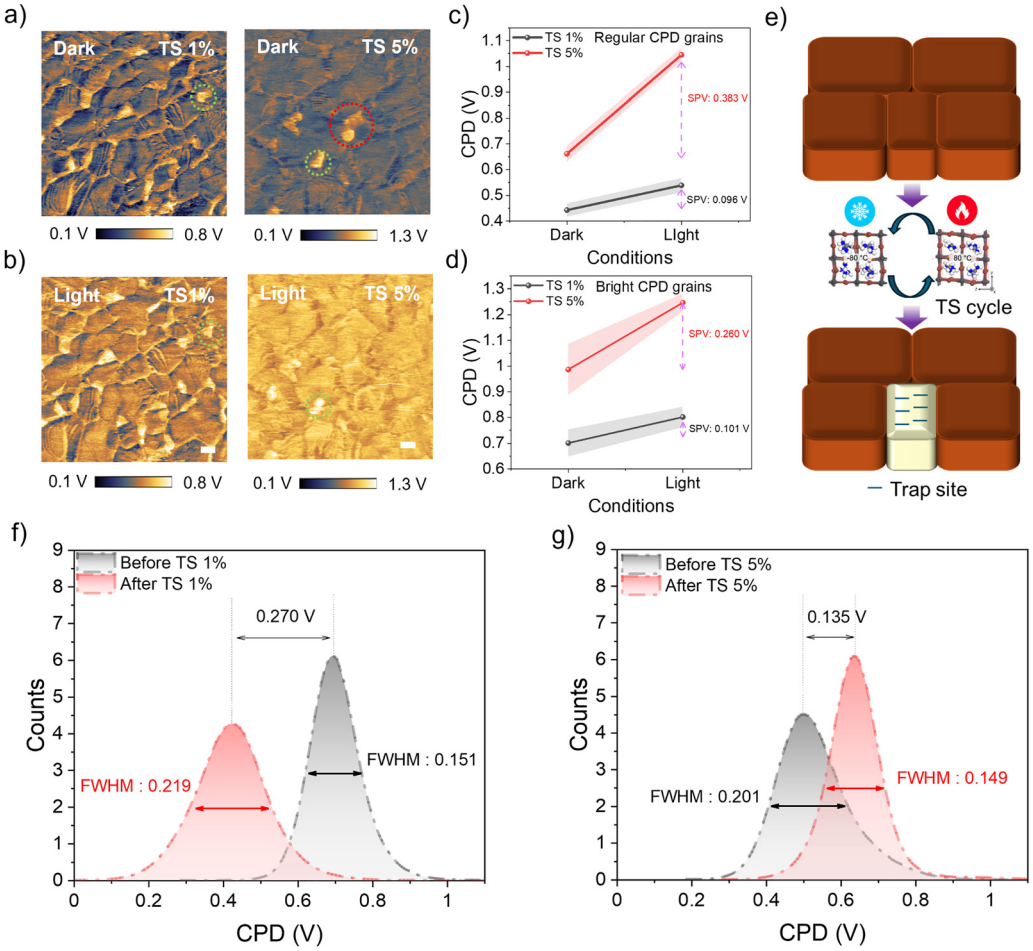

Fig. 4 KPFM images of 1% and 5% $MAPbBr_3$ samples after TS under (a) dark and (b) green light conditions. Comparison of SPV between (c) regular CPD grains and (d) bright CPD grains of TS 1% and TS 5% samples. (e) Schematic illustration of grain transformation into trap sites after TS cycling. Mean CPD distribution curves for (f) 1% and (g) 5% samples before and after TS in dark.

stability of the perovskite structure, leading to the formation of the recombination sites in the film. However, the 5% $MAPbBr_3$ sample demonstrates better phase stability and electronic uniformity under TS conditions. Additional results for other $MAPbBr_3$ concentrations are provided in Fig. S15. To further validate these findings, the work function of the perovskite films was examined using UPS, as shown in Fig. S16. The UPS data revealed that the work function changed significantly after TS for samples for 1% $MAPbBr_3$, whereas no noticeable changes were observed for the 5% $MAPbBr_3$ samples. This stability in work function at 5% $MAPbBr_3$ concentrations suggests enhanced prevention of the activation of trap states under thermal stress. This aligns with the reduced CPD shift and FWHM variation observed in the 5% $MAPbBr_3$ sample, indicating improved electronic uniformity and resistance to TS-induced degradation.

After characterizing the perovskite films post TS, we confirmed that the 5% $MAPbBr_3$ sample exhibited the least degradation among the tested compositions. To further understand the impact of TS on complete PSCs, we fabricated full devices with the architecture ITO/SnO_2/$(FAPbI_3)_{0.95}(MAPbBr_3)_{0.05}$/PEAI/PTAA/Au, encapsulated in vacuum to prevent moisture-induced degradation. Although the devices were sealed in vacuum bags, the thermal shock chamber was operated at atmospheric pressure with active airflow. Furthermore, the encapsulated devices were mounted on a metallic tray to ensure efficient thermal conduction. The polymer-based vacuum packaging exhibited minimal thermal insulation, thereby enabling effective heat transfer between the chamber environment and the device stack, as shown in Fig. S17. These devices were subjected to 100 TS cycles between ±80 °C, as illustrated in Fig. 5a. As shown in Fig. 5b, the 5% $MAPbBr_3$ sample retained approximately 80% of its original power conversion efficiency (PCE) after TS, whereas the 1% sample experienced a substantial reduction of around 38%. The corresponding reverse-scan *J–V* curves (Fig. 5c and d), along with the full parameter summary in Fig. S18 and Table S4, reveal a general decline in performance across both compositions due to TS-induced stress. Notably, the 1% sample exhibited the most pronounced deterioration, particularly in short-circuit current density (J_{SC}) and fill factor (FF), suggesting increased charge recombination and impaired charge extraction.

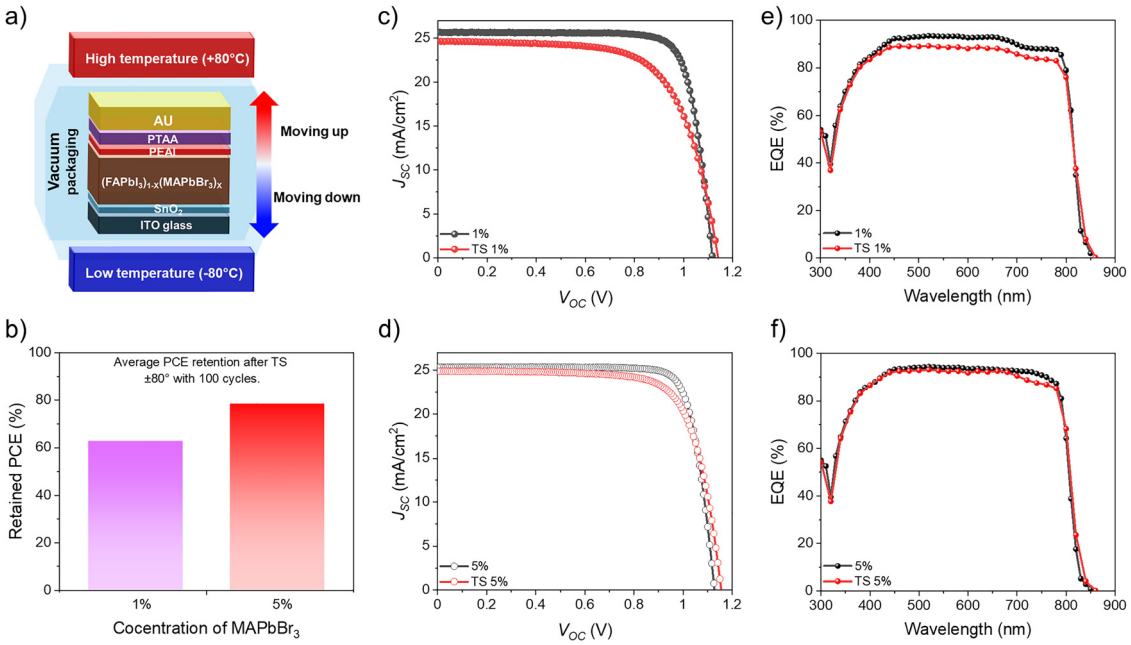

Fig. 5 (a) Schematic of the full perovskite solar cell device subjected to TS test. (b) Average PCE retention after TS for the 1% and 5% $MAPbBr_3$ samples. (c) and (d) Reverse-scan J–V characteristics of the (c) 1% and (d) 5% $MAPbBr_3$ devices before and after TS. (e) and (f) External quantum efficiency (EQE) spectra of the (e) 1% and (f) 5% $MAPbBr_3$ devices before and after TS.

While both compositions showed a reduction in J_{SC} after TS, the 5% sample maintained relatively higher values than 1% sample, indicating less TS degradation. Interestingly, the V_{OC} for both samples increased slightly after TS, which may indicate localized suppression of non-radiative recombination, potentially due to thermally induced ion redistribution.[40] This interpretation is supported by steady-state photoluminescence (PL) measurements (Fig. S19), which show an increase in PL intensity after TS for both samples. However, the concurrent decrease in FF and J_{SC} suggests an increase in series resistance and degraded charge transport pathways. Under steady-state power output tracking over 600 s, the 5% $MAPbBr_3$ device exhibits a PCE change of −2.87%, whereas the 1% device drops by −4.58%, indicating better TS resistance of the 5% sample as shown in Fig. S20.

In addition, hysteresis analysis showed that the hysteresis index of the 5% $MAPbBr_3$ device decreased to 8.27 after TS, compared to 13.03 for the 1% device. This reduction suggests improved charge transport, reduced ion migration, and enhanced device stability in the 5% sample under thermal stress. The external quantum efficiency (EQE) spectra before and after TS further corroborate these trends. As shown in Fig. 5e, the TS 1% device exhibits a substantial EQE drop across the entire visible spectrum, consistent with increased defect density and phase degradation. In contrast, the TS 5% device retains relatively stable EQE, with only a moderate decline observed in the long-wavelength region (700–800 nm) (Fig. 5f). This long-wavelength reduction may be attributed to interfacial thermal expansion mismatch between the perovskite and PTAA layers. While this phenomenon is beyond the scope of this study, future investigations should explore interfacial mechanical compatibility as a strategy for improving PSC stability under thermal extremes.

Following the TS test on complete PSC devices, we conducted a high-altitude balloon (HAB) test on October 5th, 2023, in collaboration with the Space Systems Laboratory at the University of Pisa, to evaluate the resilience and performance of PSCs under near-space conditions. The HAB ascended to an altitude of approximately 35 km, simulating the extreme environmental conditions found in near space (20–100 km), where significant temperature fluctuations and irradiance variations occur. Although the "edge of space" is conventionally defined at 100 km, the environmental conditions at 30–35 km closely resemble those found in space, as shown in Fig. 6a. At this altitude, atmospheric pressures drop to about 2% of sea level values, and densities decrease to 1.5% of their sea level counterparts.[41] This near-space environment presents a unique thermal challenge, as ambient temperatures in the stratosphere can drop to approximately −40 °C, while convective heat loss is negligible due to the low air density.[42] Additionally, direct solar exposure can cause payload surfaces to heat up beyond ground-level temperatures, creating a demanding thermal environment similar to that experienced by CubeSats in LEO. The summarized conditions of 35 km altitude in Table S5. In the HAB experiment, altitude serves as a proxy for multiple concurrent stressors, low pressure (5.6 mbar),[43] AM0 irradiance, elevated UV,[44] and temperature variation, which indicate the trends *versus* altitude reflect combined environmental loading rather than temperature alone as shown in Fig. 6b. These conditions make HABs an invaluable tool for testing and validating space-bound technologies, such as PSCs.

Fig. 6c illustrates the altitude progression during the flight. As shown in Fig. S21, the balloon reached its maximum altitude

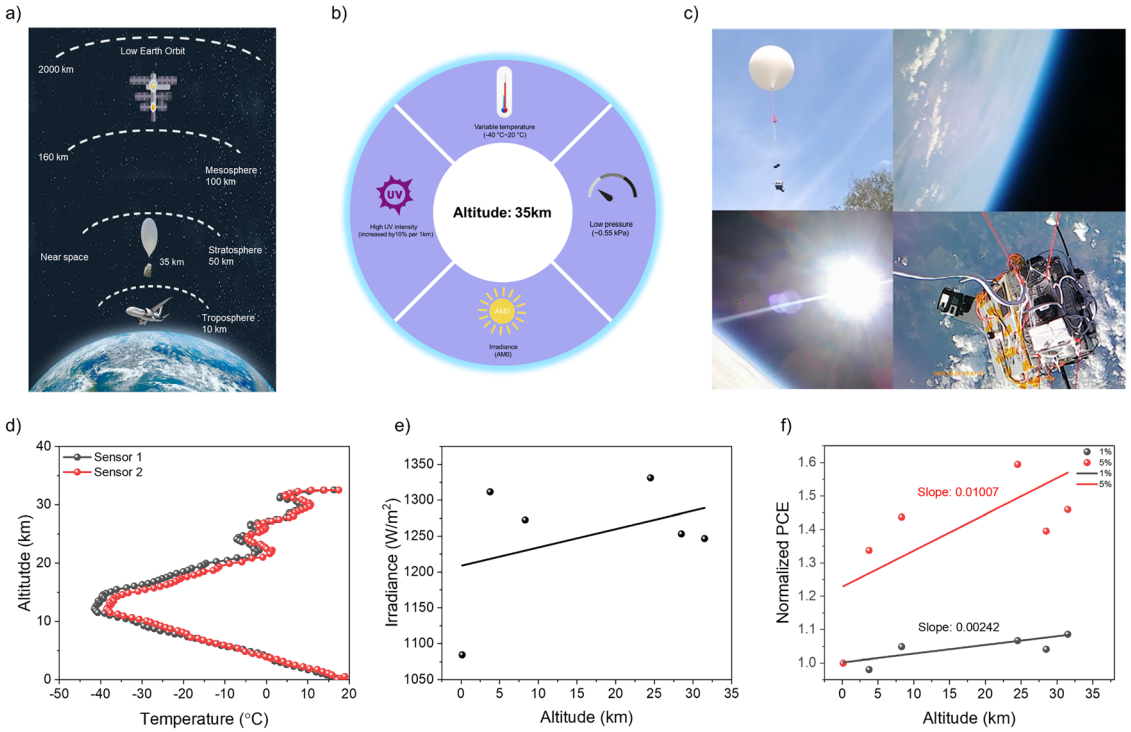

Fig. 6 (a) Schematic of the altitude where we tested HAB. (b) Summary of environmental conditions at around 35 km altitude. (c) Schematic of the HAB test. (d) Temperature-altitude plot for the two different PSCs used. (e) Measured irradiance *versus* altitude recorded during the HAB flight. (f) PCE of 1% and 5% $MAPbBr_3$ samples at different altitudes.

of 35 km approximately 1 hour and 20 minutes after launch, maintained this altitude briefly, and then descended, completing the flight in 2 hours and 20 minutes. During the ascent, temperatures drop to approximately −40 °C at 15 km and gradually stabilize in the stratosphere, where the ozone layer absorbs high-energy UV radiation, converting it into heat. The estimated steepest temperature variation rate during the ascent was approximately 2.1 °C min^{-1} (up to around 10 km altitude 20 °C to −40 °C). Temperature was monitored using two sensors attached to separate PSCs, yielding an average discrepancy of only 0.4 °C, as shown in Fig. 6d, demonstrating the reliability of the experimental setup. Additionally, irradiance data as a function of altitude, presented in Fig. 6e, further characterizes the HAB's environmental conditions. These data establish a rigorous real-world testing framework, reinforcing the relevance of PSC evaluation for future space missions.

Figure S22 displays the device performance parameters, including J_{SC}, V_{OC}, and FF, for the 1% and 5% $MAPbBr_3$ devices encapsulated with a polyisobutylene full-cover seal (Fig. S23) during the HAB test. The initial PCE measured under AM1.5 in the lab is shown in Table S6, and the corresponding absolute values during the HAB test are summarized in Table S7. The lower absolute in-flight PCE, compared to laboratory, is attributed to the constraints of the experimental platform, specifically the absence of active solar tracking and non-ideal incidence angles during flight. Nevertheless, the primary objective of this flight was to validate the relative stability differences between compositions under real near-space stressors rather than to maximize absolute power output. Data is averaged over two devices per composition. The irradiance linearly increases with altitude (Fig. 6e), suggesting that J_{SC} should follow a similar trend. However, J_{SC} does not increase linearly, particularly in the 1% sample, where the slope of J_{SC} (0.00016) is significantly lower than that of the 5% sample (0.00364), as shown in Fig. S21. This discrepancy suggests that the 1% sample suffers from severe non-radiative recombination, as confirmed by KPFM measurements, which indicate lower SPV values as shown in Fig. 4c and d. This enhanced recombination arises from defect states at grain boundaries, which trap charge carriers and inhibit efficient charge extraction. Additionally, carrier accumulation at these defect sites or transport layers can lead to electric field screening, further reducing charge separation efficiency. These findings align with EQE measurements (Fig. 5d and e), where the 1% sample exhibits the most significant drop in J_{SC}, confirming its increased recombination losses. In contrast, the 5% $MAPbBr_3$ sample demonstrates higher SPV and EQE, resulting in a steeper J_{SC} slope with increasing irradiance and reduced recombination losses. Similarly, the V_{OC} and FF of the 5% sample exhibit greater stability, with fewer fluctuations, whereas the 1% sample undergoes pronounced lower performance. Consequently, the normalized PCE, as presented in Fig. 6f, shows that the 1% sample has a lower slope (0.00032) compared to 5% (0.00565), reinforcing the improved operational stability of the 5% sample.

The overall stability performance of the 5% $MAPbBr_3$ sample across all metrics highlights its suitability for extreme

environments, such as high-altitude or space applications, where temperature and pressure variations pose significant challenges. These findings not only demonstrate the importance of TS testing for perovskite structural stabilization but also emphasize the critical need to optimize material compositions for real-world conditions.

Conclusion

In this study, we establish a novel framework for evaluating the feasibility of PSCs for space applications, emphasizing TS testing as a crucial tool for assessing phase stability and material performance under extreme conditions. Unlike standard thermal cycling protocols, TS testing for PSCs remains undefined, necessitating a systematic approach. To address this gap, we compared our TS conditions with both established thermal cycle standards and the real temperature variations experienced by satellites in LEO, which do not reach the theoretical extremes. Based on these comparisons, we propose a TS protocol of −80 °C to 80 °C at a rate of 16 °C min^{-1}, which exceeds the calculated orbital temperature fluctuation rates. This accelerated stress test effectively simulates the abrupt thermal transitions encountered in space, enabling the identification of latent failure modes.

Furthermore, we highlight the significance of phase stability in perovskite materials for enduring extreme environmental stress. Controlled incorporation of $MAPbBr_3$ into $FAPbI_3$ enhances structural resilience, not only under the intensified thermal fluctuations of our TS protocol but also under the multi-factor space-like conditions encountered during HAB testing. While the HAB temperature ramp rate differs from that of the TS protocol, it exposes devices to additional stressors, such as reduced atmospheric pressure, increased UV intensity, and AM0-like irradiance, that are highly relevant to space operation. By combining accelerated TS testing with HAB experiments, we provide a more complete evaluation of PSC structural integrity and operational stability under realistic environmental challenges. We confirm that phase stabilization is a prerequisite for TS durability, and future studies will benchmark alternative stabilizers to elucidate their responses to thermal-shock stress. Furthermore, we recognize that while this work focused on bulk microstrain, interfacial thermal expansion mismatch and macrostrain are critical factors governing failure mechanics. These aspects, including detailed characterization of coefficients of thermal expansion (CTE) and layer delamination, are essential subjects for future investigation. This is particularly relevant for the advancement of complex multilayer architectures, such as perovskite-silicon tandems, where significant CTE disparities between constituent materials can induce severe thermomechanical stress. In addition, post-flight characterization of HAB-exposed devices will be pursued to disentangle multi-stressor effects at high altitude.

These insights can inform the development of qualification protocols for perovskite panels intended for orbital photovoltaic power generation. In geostationary orbit (GEO), near-continuous solar illumination imposes sustained thermal loading and long-term radiation exposure, whereas LEO subject devices to frequent sunlit/eclipsed transitions and rapid temperature excursions. The combined use of accelerated thermal shock testing and high-altitude balloon experiments captures complementary aspects of these environments, providing a basis for tailoring material compositions and device architectures to the distinct operational demands of GEO and LEO, and thereby advancing the reliable, efficient deployment of perovskite solar technology for space power systems.

Conflicts of interest

The authors declare no conflict of interest.

Data availability

The data supporting this article have been included as part of the supplementary information (SI).

Supplementary information is available. See DOI: https://doi.org/10.1039/d5ee03704b.

Acknowledgements

J. S. Y. acknowledges the Royal Society research grant (RGS/R1/221369). This work was supported by Learning & Academic research institution for Master's PhD students, and Postdocs (LAMP) Program of the NRF grant funded by the Ministry of Education (No. RS-2023-00301974). H. H. P. and G. K. A. acknowledge support by the National R&D Program through the NRF funded by the Ministry of Science and ICT (No. 2022K1A4A8A02079724) and by the Korea Research Institute of Chemical Technology (No. KS2622-20). This work was also supported by the National Research Foundation of Korea (NRF) grant funded by the Korean government (MEST) (RS-2023-00257494). H. H. P. acknowledges that this work was supported by the Korea Institute of Energy Technology Evaluation and Planning (KETEP) and the Ministry of Trade, Industry & Energy (MOTIE) of the Republic of Korea (No. RS-2025-02309702).

References

1 Z. Li, Y. Zhao, X. Wang, Y. Sun, Z. Zhao, Y. Li, H. Zhou and Q. Chen, *Joule*, 2018, **2**, 1559–1572.
2 N. L. Chang, A. W. Yi Ho-Baillie, P. A. Basore, T. L. Young, R. Evans and R. J. Egan, *Prog. Photovoltaics Res. Appl.*, 2017, **25**, 390–405.
3 P. Čulík, K. Brooks, C. Momblona, M. Adams, S. Kinge, F. Maréchal, P. J. Dyson and M. K. Nazeeruddin, *ACS Energy Lett.*, 2022, **7**, 3039–3044.
4 J. Bing, L. G. Caro, H. P. Talathi, N. L. Chang, D. R. McKenzie and A. W. Y. Ho-Baillie, *Joule*, 2022, **6**, 1446–1474.

5 A. R. Kirmani, B. K. Durant, J. Grandidier, N. M. Haegel, M. D. Kelzenberg, Y. M. Lao, M. D. McGehee, L. McMillon-Brown, D. P. Ostrowski, T. J. Peshek, B. Rout, I. R. Sellers, M. Steger, D. Walker, D. M. Wilt, K. T. VanSant and J. M. Luther, *Joule*, 2022, **6**, 1015–1031.
6 R. S. S. Chisabas, G. Loureiro and C. de Oliveira Lino, *Space flight*, 2018, 11.
7 K. K. Degroh, B. A. Banks and D. C. Smith, Environmental durability issues for solar power systems in low earth orbit, NASA Technical Memorandum (NASA-TM-106775), United States, 1994.
8 J. J. Smithrick, *Effects of thershock cycling on thin-film cadmium sulfide solar cells*, National Aeronautics and Space Administration, Cleveland, Ohio (USA). Lewis Research Center, United States, 1969.
9 B. Jaeckel, G. Volberg, J. Althaus, G. Kleiss, P. Seidel, M. Beck and A. Roth, Safety of Photovoltaic Modules–an Overview of the Significant Changes Resulting from Maintenance of IEC 61730 Series, 29th European Photovoltaic Solar Energy Conference, 2014.
10 G. Li, Z. Su, L. Canil, D. Hughes, M. H. Aldamasy, J. Dagar, S. Trofimov, L. Wang, W. Zuo, J. J. Jerónimo-Rendon, M. M. Byranvand, C. Wang, R. Zhu, Z. Zhang, F. Yang, G. Nasti, B. Naydenov, W. C. Tsoi, Z. Li, X. Gao, Z. Wang, Y. Jia, E. Unger, M. Saliba, M. Li and A. Abate, *Science*, 2023, **379**, 399–403.
11 G. Li, Z. Su, M. Li, H. K. H. Lee, R. Datt, D. Hughes, C. Wang, M. Flatken, H. Köbler, J. J. Jerónimo-Rendon, R. Roy, F. Yang, J. Pascual, Z. Li, W. C. Tsoi, X. Gao, Z. Wang, M. Saliba and A. Abate, *Adv. Energy Mater.*, 2022, **12**, 2202887.
12 M. E. Bush, J. D. Sims, S. S. Erickson, K. T. VanSant, S. Ghosh, J. M. Luther and L. McMillon-Brown, *Acta Astronautica*, 2025, **235**, 235–250.
13 NOAA-STAR, NOAA-21 satellite data, https://ncc.nesdis.noaa.gov/NOAA-21/index.php).
14 Y. Shen, T. Zhang, G. Xu, J. A. Steele, X. Chen, W. Chen, G. Zheng, J. Li, B. Guo, H. Yang, Y. Wu, X. Lin, T. Alshahrani, W. Yin, J. Zhu, F. Wang, A. Amassian, X. Gao, X. Zhang, F. Gao, Y. Li and Y. Li, *Nature*, 2024, **635**, 882–889.
15 M. Chen, Y. Dong, Y. Zhang, X. Zheng, G. R. McAndrews, Z. Dai, Q. Jiang, S. You, T. Liu, S. P. Harvey, K. Zhu, V. Oliveto, A. Jackson, R. Witteck, L. M. Wheeler, N. P. Padture, P. J. Dyson, M. D. McGehee, M. K. Nazeeruddin, M. C. Beard and J. M. Luther, *ACS Energy Lett.*, 2024, **9**, 2582–2589.
16 Y. Li, Z. Chen, B. Yu, S. Tan, Y. Cui, H. Wu, Y. Luo, J. Shi, D. Li and Q. Meng, *Joule*, 2022, **6**, 676–689.
17 S. Li, Y. Jiang, J. Xu, D. Wang, Z. Ding, T. Zhu, B. Chen, Y. Yang, M. Wei, R. Guo, Y. Hou, Y. Chen, C. Sun, K. Wei, S. M. H. Qaid, H. Lu, H. Tan, D. Di, J. Chen, M. Grätzel, E. H. Sargent and M. Yuan, *Nature*, 2024, **635**, 82–88.
18 D. A. Lamb, S. J. C. Irvine, M. A. Baker, C. I. Underwood and S. Mardhani, *Prog. Photovoltaics Res. Appl.*, 2021, **29**, 1000–1007.
19 M. Bulut, *J. Therm. Anal. Calorim.*, 2021, **143**, 4341–4353.
20 F. Abdullah, K.-i Okuyama, I. Fajardo and N. Urakami, *Aerospace*, 2020, **7**, 35.
21 I. Fajardo, A. A. Lidtke, S. A. Bendoukha, J. Gonzalez-Llorente, R. Rodríguez, R. Morales, D. Faizullin, M. Matsuoka, N. Urakami, R. Kawauchi, M. Miyazaki, N. Yamagata, K. Hatanaka, F. Abdullah, J. J. Rojas, M. E. Keshk, K. Cosmas, T. Ulambayar, P. Saganti, D. Holland, T. Dachev, S. Tuttle, R. Dudziak and K.-I. Okuyama, *Aerospace*, 2019, **6**, 108.
22 M. Meftah, T. Boutéraon, C. Dufour, A. Hauchecorne, P. Keckhut, A. Finance, S. Bekki, S. Abbaki, E. Bertran, L. Damé, J.-L. Engler, P. Galopeau, P. Gilbert, L. Lapauw, A. Sarkissian, A.-J. Vieau, P. Lacroix, N. Caignard, X. Arrateig, O. Hembise Fanton d'Andon, A. Mangin, J.-P. Carta, F. Boust, M. Mahé and C. Mercier, *Remote Sens.*, 2021, **13**, 1449.
23 I. H. Cairns, C. Charles, A. G. Dempster, J. Funamoto, J. W. Cheong, W. Peacock, J. Lam, B. Osborne, W. Andrew, T. Croston, B. Southwell, R. W. Boswell, A. G. Monger, C. H. Betters, S. G. Leon-Saval, J. Bland-Hawthorn, J. Khachan, X. Wu, S. Manidis, D. Tsifakis and R. Maj, *Space Sci. Rev.*, 2020, **216**, 40.
24 M. H. B. Azami, N. C. Orger, V. H. Schulz, T. Oshiro, J. R. C. Alarcon, A. Maskey, K. Nakayama, Y. Fukuda, K. Kojima, T. Yamauchi, H. Masui, M. Cho and K. T. M, *Front. Space Technol.*, 2022, **3**, 1000219.
25 J. P. Mason, B. Lamprecht, T. N. Woods and C. Downs, *J. Thermophys. Heat Transfer*, 2018, **32**, 237–255.
26 Y. Kimoto, K. Yukumatsu, A. Goto, E. Miyazaki and Y. Tsuchiya, *Acta Astronaut.*, 2021, **179**, 695–701.
27 A. Poghosyan and A. Golkar, *Prog. Aerosp. Sci.*, 2017, **88**, 59–83.
28 E. C. F. S. Standardization, ECSS-E-ST-20-08C Photovoltaic Assemblies and Components, https://ecss.nl/standard/ecss-e-st-20-08c-photovoltaic-assemblies-and-components/, (accessed April 2023).
29 R. C. Consolo and S. K. S. Boetcher, in *Advances in Heat Transfer*, ed. J. P. Abraham, J. M. Gorman and W. J. Minkowycz, Elsevier, 2023, vol. 56, pp. 1–50.
30 D. W. Hengeveld, M. M. Mathison, J. E. Braun, E. A. Groll and A. D. Williams, *HVAC&R Res.*, 2010, **16**, 189–220.
31 Martin A. Green, Ewan D. Dunlop, M. Yoshita, N. Kopidakis, K. Bothe, G. Siefer, X. Hao and Jessica Y. Jiang, *Prog. Photovoltaics Res. Appl.*, 2025, **33**, 795–810.
32 H.-S. Kim and N.-G. Park, *Adv. Energy Mater.*, 2025, **15**, 2400089.
33 J. J. Yoo, G. Seo, M. R. Chua, T. G. Park, Y. Lu, F. Rotermund, Y.-K. Kim, C. S. Moon, N. J. Jeon, J.-P. Correa-Baena, V. Bulović, S. S. Shin, M. G. Bawendi and J. Seo, *Nature*, 2021, **590**, 587–593.
34 N. J. Jeon, J. H. Noh, W. S. Yang, Y. C. Kim, S. Ryu, J. Seo and S. I. Seok, *Nature*, 2015, **517**, 476–480.
35 D. K. LaFollette, J. Hidalgo, O. Allam, J. Yang, A. Shoemaker, R. Li, B. Lai, B. Lawrie, S. Kalinin, C. A. R. Perini, M. Ahmadi, S. S. Jang and J.-P. Correa-Baena, *J. Am. Chem. Soc.*, 2024, **146**, 18576–18585.
36 L. Wang, N. Wang, X. Wu, B. Liu, Q. Liu, B. Li, D. Zhang, N. Kalasariya, Y. Zhang, X. Yan, J. Wang, P. Zheng, J. Yang,

H. Jin, C. Wang, L. Qian, B. Yang, Y. Wang, X. Cheng, T. Song, M. Stolterfoht, X. C. Zeng, X. Zhang, M. Xu, Y. Bai, F. Xu, C. Zhou and Z. Zhu, *Adv. Mater.*, 2025, **37**, 2416150.
37 L. Guo, G. Tang and J. Hong, *Chin. Phys. Lett.*, 2019, **36**, 056201.
38 L. McGovern, M. H. Futscher, L. A. Muscarella and B. Ehrler, *J. Phys. Chem. Lett.*, 2020, **11**, 7127–7132.
39 M. Hao, J. Yang, W. Yu, B. J. Lawrie, P. Guo, X. Zhang, T. Duan, T. Xiao, L. Chen, Y. Xiang, P. Guo, M. Ahmadi and Y. Zhou, *Nat. Nanotechnol.*, 2025, **20**, 630–638.
40 Y. Zhao, J. Zhang, Z. Xu, S. Sun, S. Langner, N. T. P. Hartono, T. Heumueller, Y. Hou, J. Elia, N. Li, G. J. Matt, X. Du, W. Meng, A. Osvet, K. Zhang, T. Stubhan, Y. Feng, J. Hauch, E. H. Sargent, T. Buonassisi and C. J. Brabec, *Nat. Commun.*, 2021, **12**, 2191.
41 K. S. Lay, L. Li and M. Okutsu, *HardwareX*, 2022, **12**, e00329.
42 S. Atmosphere, ISO, 1975, **2533**, 1975.
43 U. S. C. O. E. T. T. S. Atmosphere, *US standard atmosphere*, 1976, National Oceanic and Amospheric [sic] Administration, 1976.
44 M. Blumthaler, W. Ambach and R. Ellinger, *J. Photochem. Photobiol., B*, 1997, **39**, 130–134.

